Physica Scripta

PAPER

RECEIVED
14 January 2026

REVISED
10 March 2026

ACCEPTED FOR PUBLICATION
23 March 2026

PUBLISHED
2 April 2026

Controlling the spin-wave modes in planar nanostructure with wire-ring morphology

Eduardo Saavedra[1,*], Ulises Guevara[2], Helmunt Vigo-Cotrina[3], Mohammed Al Bahri[4], Tamara González-Vega[5] and Laura M Pérez[6]

[1] Departamento de Física, Universidad de Santiago de Chile, 9170124, Santiago, Chile
[2] Vicerrectoría de Investigación y Postgrado, Universidad de La Serena, La Serena 1700000, Chile
[3] Centro de Investigación en Nanotecnología y Materiales Avanzados (CINMA), Universidad Privada del Norte (UPN), Peru
[4] Department of Basic and Applied Sciences, A'Sharqiyah University, Post Box 42, PC 400, Ibra, Oman
[5] Facultad de Ciencias de la Vida, Universidad Viña del Mar, Agua Santa 7055, Rodelillo, Viña del Mar 2572007, Chile
[6] Departamento de Ingeniería Industrial y de Sistemas, Universidad de Tarapacá, Casilla 7D, Arica 1000000, Chile
[*] Author to whom any correspondence should be addressed.

E-mail: eduardo.saavedra.d@usach.cl

Keywords: micromagnetic simulation, spin-wave resonance, wire-ring Geometry

Supplementary material for this article is available online

Abstract

We investigate the dynamic magnetic response of planar ferromagnetic nanostructures with wire-ring morphology using micromagnetic simulations. By systematically varying the inner ring diameter and thickness, we analyze how geometric confinement governs the accessibility of stable and metastable magnetic states and shapes the spin-wave spectra. The equilibrium configurations are found to depend strongly on the relaxation pathway, giving rise to bistability for intermediate ring diameters. Dynamic susceptibility calculations under microwave excitation reveal distinct resonance spectra associated with low- and high-energy magnetic states, which we classify in terms of two energy-evolution paths. Spatial Fourier analysis of the out-of-plane magnetization identifies wire-like, ring-localized, and hybrid spin-wave modes, whose localization and spectral complexity are controlled by geometry. Our results demonstrate that planar wire-ring nanostructures offer a versatile platform for tailoring spin-wave excitations through geometric design, with potential implications for reconfigurable magnonic and spintronic devices.

1. Introduction

In recent decades, significant progress has been achieved in the understanding of both static and dynamic magnetic properties of nanoscale systems with planar geometries [1–4]. This advance has been driven by the development of lithographic techniques that enable the fabrication of ferromagnetic nanostructures with complex shapes, allowing precise control over magnetization configurations, domain-wall dynamics, and spin-wave excitations [5, 6]. Among these systems, planar ferromagnetic nanowires have attracted considerable attention because they can effectively act as conduits for the controlled propagation of domain walls [7]. As a result, they constitute the basis for a wide range of proposed applications, including magnetic logic devices [8], sensors [9], and more recently, concepts for magnetic memory technologies [10, 11].

To further manipulate domain-wall motion and magnetization reversal processes, a variety of geometric modifications have been introduced in planar nanowires, such as triangular [12, 13], rectangular [14], or asymmetric notches [15, 16], anti-notches [17], nucleation pads [18], and patterned constrictions [7, 19]. These features generate controlled pinning landscapes that allow domain walls to be nucleated, trapped, or released in a predictable manner. An alternative and particularly versatile strategy consists of integrating a nanoring within the nanowire, giving rise to planar nanostructures with wire-ring morphology [20, 21]. In these systems, the closed topology of the ring introduces additional geometric degrees of freedom—most notably the inner

diameter and wall thickness of the ring—which strongly influence the magnetic energy landscape and enable enhanced control of magnetization processes.

Recent studies have highlighted the central role of geometry in determining the static and dynamic magnetic properties of nanoscale systems. Variations in shape [22] and curvature can significantly influence the stability of magnetic configurations, including quasi-uniform and vortex states, as well as the localization and frequency of spin-wave modes. In particular, different geometries such as nanowires [23], curved nanostructures [24], and coupled systems [3] provide distinct mechanisms for controlling magnetization dynamics and resonance spectra.

However, most of these geometries are limited to either open or closed magnetic pathways, restricting the diversity of accessible magnetic states and dynamic responses. In this context, hybrid geometries that combine multiple topological features offer a promising route to achieve enhanced control over magnetic configurations and their associated spin-wave excitations.

In this context, planar wire-ring nanostructures represent a particularly versatile class of hybrid systems that combine open and closed magnetic pathways. They have been shown to support a rich variety of magnetic behaviors. Depending on the ring geometry, magnetization reversal may proceed through domain-wall nucleation and propagation along the nanowire, or through vortex formation within the ring region, leading to distinct hysteresis signatures and metastable states [20, 21, 25]. Moreover, by combining different magnetic materials in the wire and ring sections, it is possible to control the chirality of vortex domain walls as they traverse the ring, highlighting the potential of these systems for domain-wall–based logic [26] and memory applications [27].

While the static magnetic behavior and magnetization reversal mechanisms of planar wire–ring nanostructures have been widely investigated, their high-frequency dynamic response remains far less explored. In particular, the presence of multiple accessible magnetic states suggests that different relaxation pathways may lead to distinct ferromagnetic resonance spectra, an aspect that is crucial for magnonic applications but has not been systematically addressed.

The experimental realization of the proposed geometry is compatible with established top-down nanofabrication techniques. Electron-beam lithography (EBL) combined with metal deposition and lift-off or ion milling has been widely used to fabricate magnetic nanostructures with lateral dimensions below 50 nm [28]. In particular, lithographically defined magnetic nanorings have been experimentally demonstrated [29], indicating that the geometrical parameters considered here (50 nm wire width, 100 nm ring diameter, and thicknesses between 1 and 25 nm) lie within current fabrication capabilities.

Moreover, the characteristic magnetic length scales of the configurations studied here are well within the resolution limits of existing magnetic imaging techniques. Synchrotron-based x-ray magnetic circular dichroism (XMCD) microscopies, such as X-PEEM and scanning transmission x-ray microscopy (STXM), routinely achieve spatial resolutions in the 20–30 nm range [30–32], which are sufficient to resolve the magnetic configurations predicted in this work. Therefore, both fabrication and experimental observation of the proposed system are feasible with current state-of-the-art techniques.

In this work, we investigate the dynamic magnetic response of planar wire–ring nanostructures using micromagnetic simulations, focusing on the role of geometric parameters and relaxation pathways in determining the accessible magnetic states and their associated spin-wave spectra. By correlating equilibrium configurations with dynamic susceptibility and spatial mode profiles, we demonstrate how geometry enables controlled tailoring of spin-wave excitations.

2. Model and methodology

We investigate the dynamic magnetic properties for non-interacting planar nanostructures with a wire-ring morphology using the MuMax3 software [33] which solved the Landau–Lifshitz-Gilbert (LLG). The effective magnetic field includes exchange, Zeeman, and long-range magnetostatic (dipolar) interactions. As shown in figure 1 this planar nanostructure has a thickness h, which varies between 1 and 25 nm and is composed of three structures: the first is a planar nanowire with length $x_1 = 250$ nm and width $y_1 = 50$ nm. The second structure is a nanoring that has an outer diameter $D = 100$ nm and an inner diameter d variable, which in our particular case, we have varied d between 0 nm and 90 nm. The third structure is another planar nanowire with lengths $x_2 = 150$ nm and $x_3 = 100$ nm.

All of the simulations utilized a 1 nm mesh to accurately represent the geometry and to be below the characteristic exchange length of the material (in the case of Permalloy it is 5.08 nm), and employed standard magnetic parameters for Permalloy [34], including saturation magnetization of $M_s = 800 \times 10^3$ Am^{-1} and exchange stiffness of $A = 13 \times 10^{-12}$ Jm^{-1}. Magnetocrystalline anisotropy was set to $K_u = 0$ Jm^{-3}, consistent with the soft-magnetic approximation commonly adopted for Permalloy, where crystalline anisotropy is negligible. All

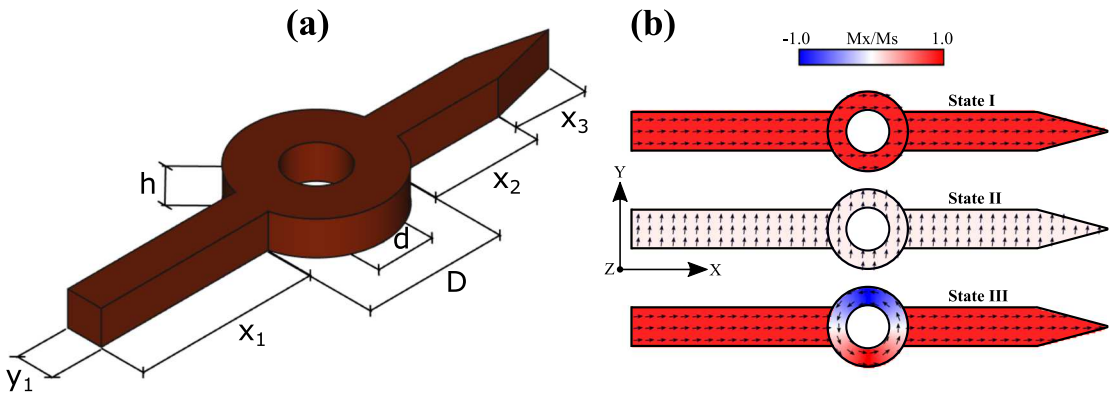

Figure 1. (a) Schematic representation of the planar ferromagnetic nanostructure with wire-ring geometry, showing the main geometric parameters. (b) Initial magnetization configurations considered before relaxation: State I with quasi-uniform magnetization along the *x* direction, State II with quasi-uniform magnetization along the *y* direction, and State III combining a vortex-like state in the ring with a longitudinally magnetized nanowire. The color scale represents the normalized magnetization component M_x/M_s.

micromagnetic simulations were performed under ideal conditions (uniform material parameters, smooth boundaries, and T = 0 K) in order to determine the intrinsic geometry-driven energy landscape of the system. In experimental realizations, structural disorder can be interpreted as spatial variations of material parameters (e.g., saturation magnetization, exchange stiffness, or anisotropy), while edge roughness primarily introduces additional pinning and quantitative shifts in switching thresholds. Finite temperature is expected to reduce effective energy barriers and modify critical fields.

These effects generally lead to quantitative variations in stability ranges and transition fields rather than suppressing geometry-stabilized local energy minima, except in cases where the system lies extremely close to a critical transition boundary. Therefore, the bistable regimes identified here are expected to remain qualitatively robust under realistic experimental conditions.

Moreover, multistability and stimulus-driven transitions between distinct magnetic states are well established experimentally in confined nanostructures. Field- and current-induced switching between vortex, onion, and other topologically distinct configurations has been demonstrated in magnetic nanorings and related systems [35–37], supporting the physical relevance of multiple local energy minima in nanoscale magnetism.

To analyze the frequency spectra of the excited system, we employed the Ringdown method [38, 39], which consists of two main steps: (i) First, the minimum energy configuration was obtained under zero external field, using a damping parameter of $\alpha = 0.5$. The simulation was halted when the torque on all magnetic moments fell below 10^{-4} T [40]. Next, a 100-nanosecond time minimization step was performed to further attenuate residual spin waves. Energy minimization was performed starting from three initial magnetic configurations: **State I**, a ferromagnetic state aligned almost entirely along the *x*-direction; **State II**, a ferromagnetic state aligned almost entirely along the *y*-direction; and **State III**, a hybrid configuration combining a vortex state in the ring with a ferromagnetic state in the nanowire aligned almost entirely along the *x*-direction. These initial configurations were chosen to probe different regions of the magnetic energy landscape that are commonly accessed during experimental magnetization reversal processes in wire-ring systems [20, 21]. The magnetization profiles are depicted in figure 1(b) respectively.

Throughout this work, we refer to two distinct relaxation pathways. **Path I** corresponds to relaxation processes that converge to the lowest-energy magnetic configuration, whereas **Path II** leads to metastable higher-energy states stabilized by geometric confinement. These paths emerge naturally from the energy landscape of the wire–ring geometry and depend on the initial magnetic configuration.

Subsequently, a sinc magnetic pulse field $\boldsymbol{h}(t) = h_0 \sin[2\pi f_{\max}(t - t_0)]\,\hat{\boldsymbol{z}}$ was applied [41, 42]. Here, the amplitude was set at $h_0 = 1$ mT, with a cut-off frequency of $f = 20$ GHz. The excitation amplitude was chosen sufficiently small to ensure a linear dynamic response and to avoid inducing irreversible changes in the magnetic configuration. The spatial profile of the z-component of the magnetization was saved every 10 ps for a total simulation time of 100 ns, and the frequency resolution was 0.01GHz. In this process, a lower damping constant $\alpha = 0.008$ was used [43, 44], a typical value for permalloy providing better resolution of the spin wave modes. Using the Fast Fourier Transform (FFT), both the excitation field $h(t)$ and the magnetization $M(t)$ were transformed to the frequency domain $[h(\omega), M(\omega)]$. The nature of the spin wave modes was determined by numerical calculations of the spatial distributions of the amplitudes of the resonances. For this purpose, we determined the time of the Fourier image of each magnetic moment $\mathrm{m}(\mathrm{r}_{ijk},\omega_n) = \mathrm{DFTt}\,(\mathrm{m}(\mathrm{r}_{ijk}, \mathrm{t}_n))$ (obtained

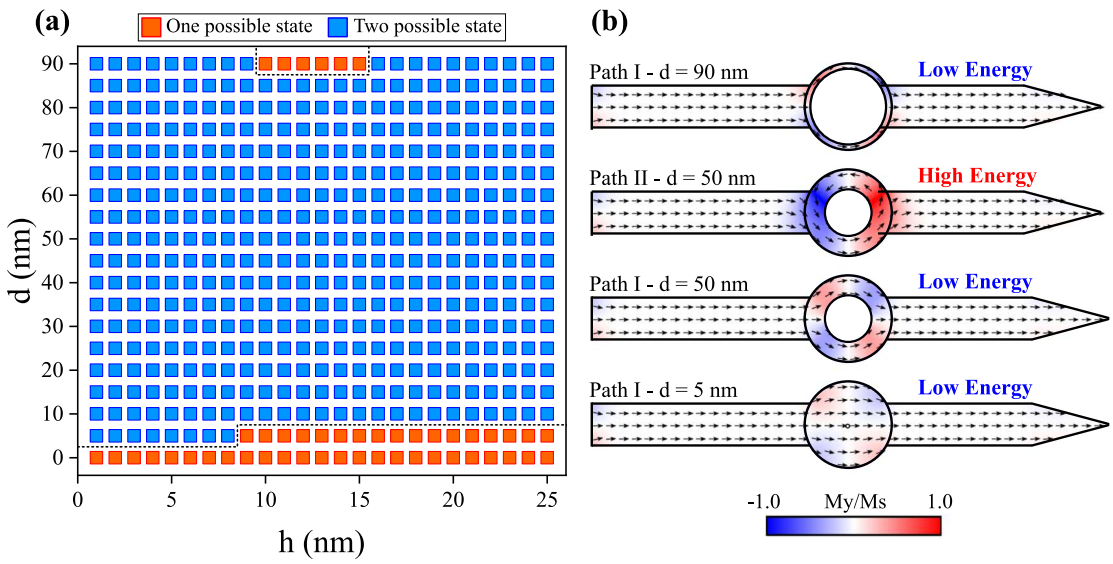

Figure 2. (a) Phase diagram as a function of the inner ring diameter d (nm) and the thickness h (nm), indicating the number of accessible equilibrium magnetic states after relaxation. Orange denotes a single possible state, while light blue indicates bistability. (b) Representative relaxed magnetic configurations for $h = 15$ nm at selected values of d, showing that Path I and Path II converge to the same low-energy state for small and large d, whereas at intermediate d they lead to distinct low- and high-energy configurations. The color scale represents M_y/M_s.

from Mumax3 simulations), where DFTt is the Fourier transform. The subscripts ijk correspond to each cell's spatial coordinates x, y, and z, while the subscript n denotes the frequency position of the power spectrum.

3. Results and analysis

The equilibrium magnetic states are determined after the relaxation process described above, starting from different initial configurations (States I, II, and III). The resulting magnetic behavior is summarized in the phase diagram shown in figure 2(a), presented as a function of the inner ring diameter d (nm) and the thickness h (nm). The color coding indicates the number of accessible magnetic states after relaxation: orange denotes a single possible final state, whereas light blue indicates bistability, corresponding to the coexistence of two distinct final states depending on the initial condition.

Figure 2(b) shows representative relaxed magnetic configurations (normalized magnetization component M_y/M_s) calculated for $h = 15$ nm at selected values of d, explicitly illustrating the role of different relaxation pathways. In all cases, and for both Path I and Path II, the magnetic moments located in the wire segments (i.e., regions x_1, x_2, and x_3) are predominantly aligned along the longitudinal axis of the nanostructure, as a consequence of the strong shape anisotropy imposed by the elongated wire geometry. For large inner diameters, relaxation along Path I and Path II leads to the same low-energy configuration, indicating a unique equilibrium state that is independent of the initial condition. In contrast, for intermediate values of d, the system exhibits bistability: relaxation along Path I results in a low-energy state in which the central ring hosts an onion-like configuration, with magnetic moments following the curved trajectory, whereas Path II drives the system toward a distinct high-energy configuration characterized by a vortex state in the ring, where the magnetization undergoes curling around the ring circumference. For very small inner diameters, both relaxation paths again converge to the same low-energy state, reflecting the dominance of geometric confinement over the relaxation dynamics.

To further elucidate the energetic origin of the different relaxation pathways, figure S1 in the Supplementary Material presents the total final energy as a function of the inner diameter d for several thickness values h, considering all three initial states. These energy curves confirm that the bistable regions identified in the phase diagram correspond to ranges of d where relaxation along Path I and Path II leads to two energetically distinct local minima. Outside these regions, the energy landscape is characterized by a single global minimum, such that both paths converge to the same equilibrium configuration regardless of the initial state.

In addition, figures S2 and S3 in the Supplementary Material present representative relaxed magnetic configurations for the extreme thickness values $h = 1$ nm and $h = 25$ nm, respectively, at selected inner diameters d. These results demonstrate that the qualitative features identified for $h = 15$ nm specifically, the convergence of

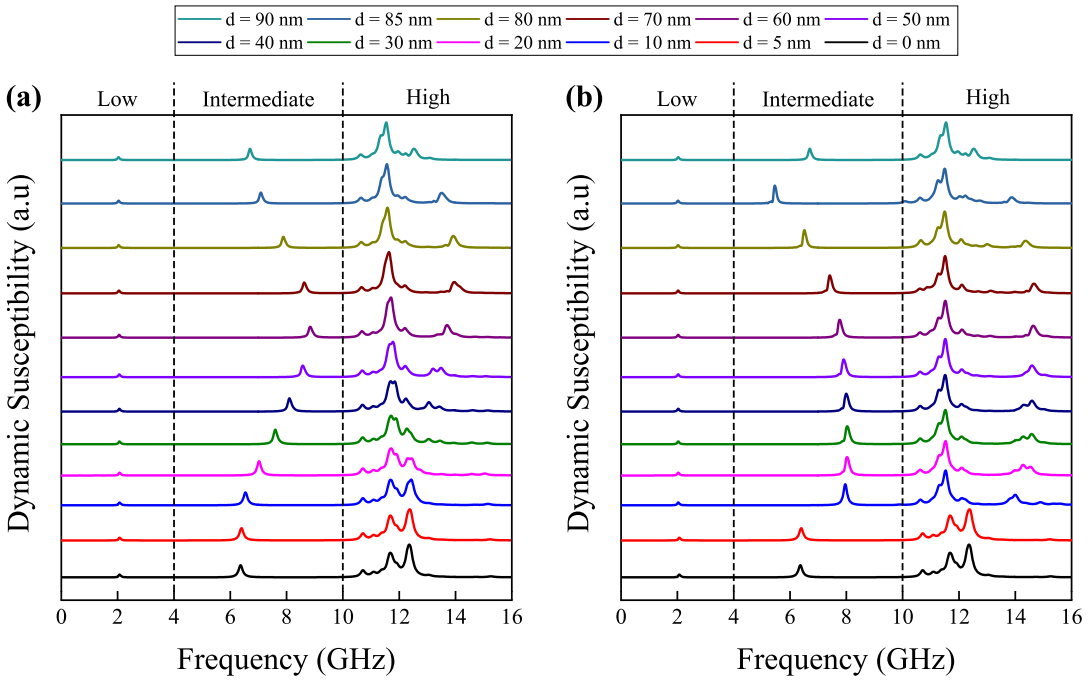

Figure 3. Dynamic susceptibility spectra of planar wire-ring nanostructures with a thickness of $h = 15$ nm for varying inner ring diameters d. The spectra illustrate two distinct energy-evolution trajectories: (a) Path I and (b) Path II. In all configurations, the magnetic field pulse is applied perpendicular to the nanostructure plane. Dashed vertical lines demarcate the low-, intermediate-, and high-frequency regimes.

Path I and Path II to a unique low-energy state for small and large d, and the emergence of bistability at intermediate inner diameters-remain robust over a broad range of thicknesses.

After establishing the stable and metastable magnetic configurations as a function of the inner ring diameter d and thickness h, we investigate the dynamic magnetic response of the system under an out-of-plane magnetic field pulse applied along the z direction, following the procedure described in the Model and Methodology section. The resulting dynamic magnetic susceptibility spectra for planar wire-ring nanostructures with $h = 15$ nm and varying d are presented in figure 3, where panels (a) and (b) correspond to Path I and Path II, respectively, and the dashed vertical lines separate the spectra into low-, intermediate-, and high-frequency regimes to facilitate the interpretation of the collective behavior of the resonant frequencies.

For Path I [figure 3(a)], the dynamic susceptibility spectra exhibit a well-defined set of resonant modes that are largely preserved over the entire range of inner diameters. A single resonance is observed in the low-frequency regime, together with a second isolated mode in the intermediate-frequency region. In contrast, the high-frequency regime displays a more complex modal structure, with up to eight distinct resonant modes appearing between approximately 10 and 15 GHz.

As the inner diameter decreases, the low-frequency mode remains essentially unchanged, indicating a weak sensitivity to geometric confinement. The intermediate-frequency mode, however, exhibits a non-monotonic behavior, characterized by small frequency shifts and amplitude variations that reflect a redistribution of the dynamic magnetization. In the high-frequency regime, the resonant modes undergo a weak and nearly monotonic downward frequency shift while preserving their relative spectral ordering and comparable intensities.

For Path II [figure 3(b)], the dynamic susceptibility spectra preserve the overall modal organization observed for Path I, with one dominant resonance in the low-frequency regime, a single well-defined mode in the intermediate-frequency range, and a complex structure in the high-frequency regime. As in Path I, up to eight resonant modes are observed between approximately 10 and 16 GHz, indicating that the total number of accessible spin-wave modes is largely insensitive to the relaxation path.

Despite these similarities, clear differences emerge in the detailed spectral evolution. Compared to Path I, the intermediate-frequency mode in Path II exhibits larger frequency shifts and more pronounced variations in amplitude as the inner diameter decreases, revealing a stronger sensitivity to the underlying magnetic configuration. In the high-frequency regime, although the resonant modes follow a similar weak downward frequency shift with decreasing inner diameter, Path II displays broader resonances and noticeable changes in the relative peak intensities among neighboring modes.

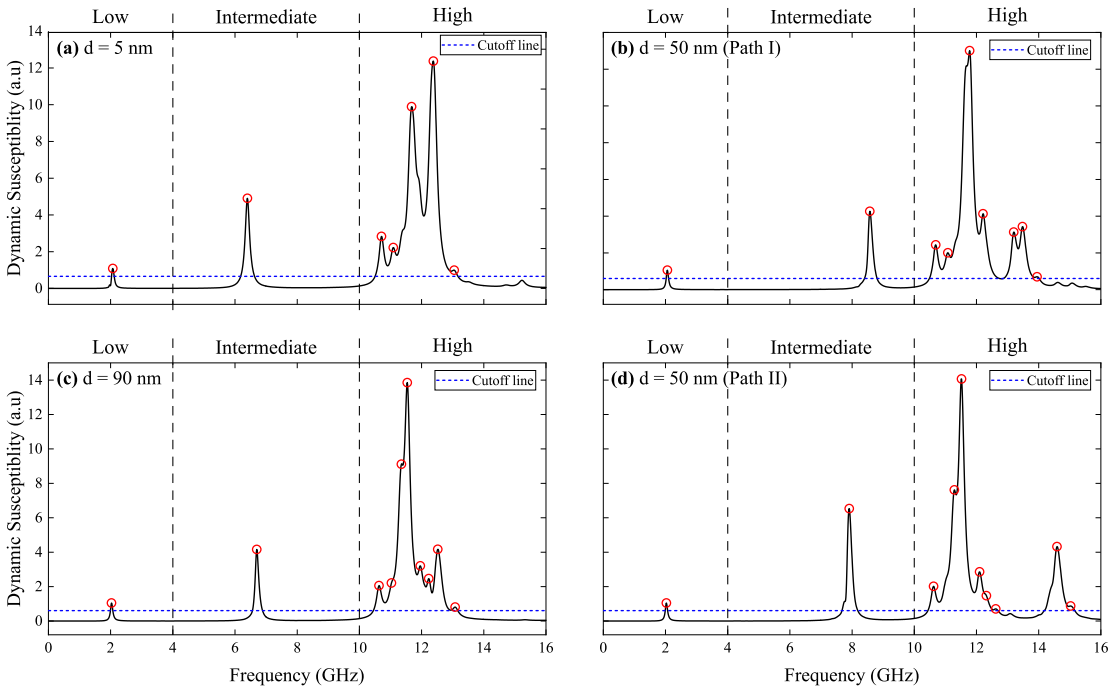

Figure 4. Dynamic susceptibility spectra of planar wire–ring nanostructures with thickness h=15 nm for different inner ring diameters d. Panels correspond to (a) d = 5 nm, (b) d = 50 nm following Path I, (c) d = 90 nm, and (d) d = 50 nm following Path II. In all cases, the magnetic field pulse is applied perpendicular to the nanostructure plane. Dashed vertical lines delineate the low-, intermediate-, and high-frequency regimes. The horizontal dashed blue line indicates the cutoff threshold used to identify resonant modes, which are highlighted by red circles.

To evaluate the robustness of the higher-energy configuration against thermal activation, additional simulations including thermal fluctuations at T = 300 K were performed for h = 15 nm within the bistable diameter range (d = 10–80 nm). Figure S4 in the Supplementary Material compares the dynamic susceptibility spectra obtained at T = 0 K and T = 300 K for the high energy configuration. Although thermal fluctuations introduce stochastic noise and moderate spectral broadening, the resonance positions and overall modal structure remain clearly preserved.

Figure 4 provides a detailed view of the dynamic magnetic susceptibility spectra for selected inner ring diameters d at a fixed thickness $h = 15$ nm, highlighting the identification of individual resonant modes across different frequency regimes. The cutoff threshold, defined as 4% of the amplitude of the highest-intensity resonance among all analyzed spectra, was used to ensure a consistent and simplified identification of the dominant modes. This threshold is indicated by the horizontal dashed blue line, while the identified resonant peaks are highlighted by red circles.

For small inner diameters [figure 4(a), $d = 5$ nm] and large inner diameters [figure 4(c), $d = 90$ nm], the spectra are associated with a unique low-energy magnetic configuration, resulting in a well-defined and reproducible set of resonant modes dominated by the high-frequency regime. In contrast, for the intermediate diameter $d = 50$ nm, the dynamic magnetic susceptibility depends strongly on the relaxation pathway. As shown in figure 4(b), relaxation along Path I yields a spectrum with fewer intense high-frequency resonances and a more regular modal structure. Conversely, relaxation along Path II [figure 4(d)] leads to a richer high-frequency spectrum with additional resonant peaks and enhanced intensities, reflecting the metastable, higher-energy magnetic configuration.

Considering that edge roughness in experimentally fabricated nanostructures may introduce additional pinning and contribute to resonance line-width broadening, we assessed the robustness of our results through simulations with increased in-plane discretization. As shown in figure S5 in the Supplementary Material, only moderate peak broadening and slight frequency shifts are observed, and the vortex state remains stable across all tested conditions.

To elucidate the origin of the resonant peaks identified in figure 4 and to gain deeper insight into the role of geometric confinement, figure 5 presents the spatial profiles of the excited spin-wave modes extracted from the Fourier transform of the out-of-plane magnetization component M_z. For the small inner diameter case ($d = 5$ nm), seven distinct resonant modes are identified within the analyzed frequency range, each characterized by a unique spatial distribution of the dynamic magnetization.

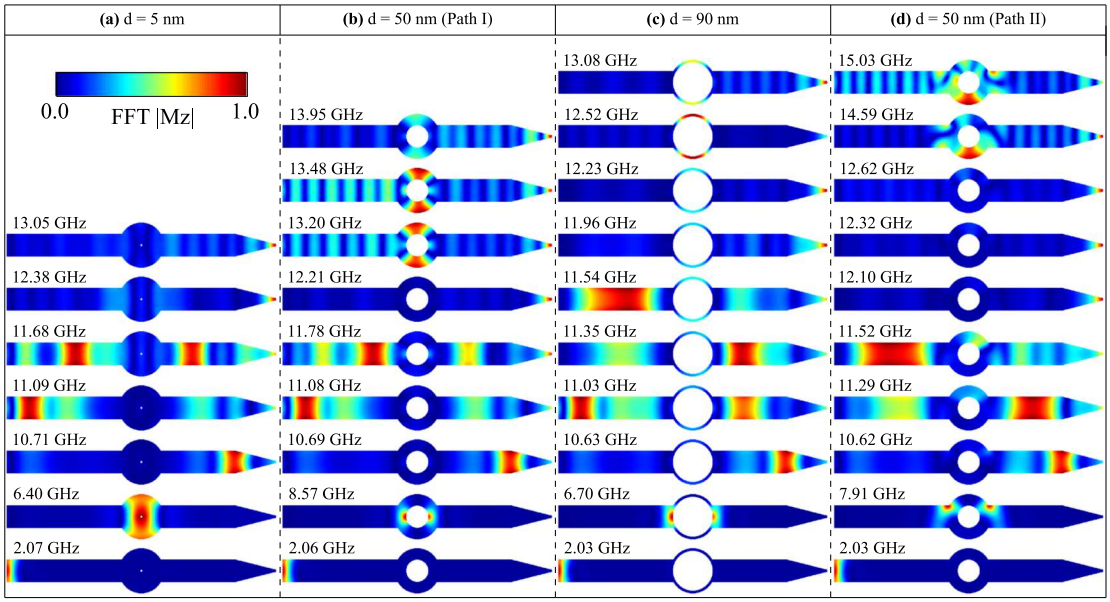

Figure 5. Spatial profiles of the excited spin-wave modes obtained after applying a small microwave magnetic field pulse perpendicular to the nanostructure plane. Columns correspond to different inner ring diameters and energy-evolution paths: (a) $d = 5$ nm, (b) $d = 50$ nm (Path I), (c) $d = 90$ nm, and (d) $d = 50$ nm (Path II). Rows display representative resonant modes at the indicated frequencies. The color scale represents the normalized amplitude of the FFT of the out-of-plane magnetization component M_z, where red (blue) indicates higher (near-zero) spin-wave amplitude. (For interpretation of the references to color in this figure legend, the reader is referred to the web version of this article.).

The lowest-frequency mode, at approximately 2.07 GHz, is weakly excited and exhibits magnetization oscillations localized at the left edge of the nanowire, along the longitudinal segment x_1. The mode at 6.40 GHz displays a strong localization of the dynamic oscillations within the ring region, with an almost symmetric amplitude distribution around the ring, indicating a ring-confined spin-wave mode. In the high-frequency regime (approximately 10-16 GHz), the resonant modes are predominantly extended along the nanowire, forming standing-wave patterns characterized by multiple antinodes distributed along the wire length. Notably, the modes at 12.38 GHz and 13.05 GHz exhibit localized excitation at the right edge of the nanostructure (right edge of the longitudinal segment x_3), while the central wire region simultaneously supports standing-wave-like oscillations [3, 45–47].

For the intermediate inner diameter case ($d = 50$ nm), the spatial profiles of the resonant modes exhibit a strong dependence on the relaxation pathway, reflecting the bistable nature of the magnetic configuration. Along Path I, the dominant modes are relatively delocalized along the nanowire, forming standing-wave patterns with well-defined nodes and antinodes, while the contribution of the ring region to the overall dynamic response remains weak and becomes noticeable only at specific frequencies, such as 8.57 GHz, 13.20 GHz, 13.48 GHz, and 13.95 GHz. These modes closely resemble those observed for small inner diameters, consistent with the stabilization of a low-energy magnetic configuration.

In contrast, along Path II, the spatial profiles reveal a markedly different behavior. Several resonant modes exhibit pronounced localization around the ring, accompanied by asymmetric intensity distributions and enhanced dynamic oscillations near the wire-ring junctions, as observed, for instance, at 7.91 GHz and 11.52 GHz. At higher frequencies, the modes display a mixed character, combining ring-localized oscillations with standing-wave patterns extending along the nanowire.

In the high-frequency regime, spanning approximately 10 to 13.1 GHz, the resonant modes are mainly extended along the nanowire and form well-defined standing-wave patterns characterized by multiple antinodes distributed along its length. Several modes, including those at 10.63, 11.03, and 11.35 GHz, exhibit a systematic increase in the number of nodes as the frequency rises, which is consistent with higher-order spin-wave excitations imposed by geometric confinement [3, 47, 48]. The mode at 11.54GHz shows enhanced intensity localized near the left side of the nanowire, while modes at higher frequencies, between 12.23 and 13.08 GHz, present a more homogeneous spatial distribution with only weak modulation around the ring [49, 50]. These differences can also be interpreted in terms of the demagnetizing field, shown in figure S6 in the Supplementary Material. From the analysis of these results, it is evident that for $d = 50$ nm the stray field associated with Path II exhibits a multipolar-like structure, arising from the presence of a vortex state hosted in the central ring. This multipolar character is absent in the $d = 50$ nm configuration obtained along Path I, where the ring remains in an onion-like state. The distinct spatial distributions of the demagnetizing field in the

two cases lead to different internal field landscapes, which in turn account for the emergence and redistribution of resonant spin-wave modes observed for Path I and Path II.

The geometric transition between the wire and the ring introduces a localized modification of the effective magnetic field, including the demagnetizing contribution, which may in principle influence spin-wave reflection and transmission in a propagative regime. However, the present work focuses on the intrinsic eigenmodes of the coupled wire–ring system, obtained from full micromagnetic simulations in which the dipolar field is computed self-consistently. Therefore, the reported hybrid modes inherently incorporate the effects of the junction, while a quantitative analysis of magnonic transport, reflection coefficients, or impedance mismatch lies beyond the scope of this study.

For the large inner diameter case ($d = 90$ nm), the spatial profiles of the resonant modes indicate the presence of a unique and stable low-energy magnetic configuration. The lowest-frequency mode, at approximately 2.03 GHz, exhibits localized oscillations at the left edge of the nanowire, characteristic of an edge-like excitation. At 6.70 GHz, the dynamic magnetization becomes weakly confined around the ring region, revealing a low-order ring-assisted mode.

In the high-frequency regime, spanning approximately 10 to 13.1 GHz, the resonant modes are mainly extended along the nanowire and form well-defined standing-wave patterns characterized by multiple antinodes distributed along its length. Several modes, including those at 10.63, 11.03, and 11.35 GHz, exhibit a systematic increase in the number of nodes as the frequency rises, which is consistent with higher-order spin-wave excitations imposed by geometric confinement [3, 47, 48]. The mode at 11.54GHz shows enhanced intensity localized near the left side of the nanowire, while modes at higher frequencies, between 12.23 and 13.08 GHz, present a more homogeneous spatial distribution with only weak modulation around the ring [49, 50].

4. Conclusions

In this work, we have presented a comprehensive micromagnetic investigation of the static and dynamic magnetic properties of planar ferromagnetic nanostructures with wire–ring morphology. By systematically varying the inner ring diameter and thickness, we have shown that geometric confinement plays a decisive role in shaping both the equilibrium magnetic configurations and the associated spin-wave response.

Our results demonstrate the existence of distinct relaxation pathways leading either to a unique low-energy magnetic state or to bistable regimes in which low- and high-energy configurations coexist for intermediate inner ring diameters. This bistability is robust over a wide range of thicknesses and originates from the geometric constraints imposed by the wire–ring architecture. Importantly, the different equilibrium states are characterized by markedly different internal field landscapes, as evidenced by the distinct spatial distributions of the demagnetizing field.

The dynamic susceptibility analysis reveals that, although the total number of accessible resonant modes remains largely unchanged, the relaxation pathway strongly influences the spectral distribution, intensity, and spatial localization of the spin-wave modes. Spatial Fourier analysis identifies a rich variety of excitations, including edge-localized modes, ring-confined resonances, extended standing-wave modes along the nanowire, and hybrid modes arising from the coupling between wire and ring regions. These features highlight the strong correlation between magnetic state, internal field topology, and dynamic response.

Overall, our findings establish planar wire–ring nanostructures as a versatile and reconfigurable platform for controlling spin-wave excitations through geometric design and magnetic state selection. The demonstrated sensitivity of the spin-wave spectra to relaxation pathways provides a promising route toward state-selective and geometry-driven functionality in future magnonic and spintronic devices based on complex planar nanogeometries.

Acknowledgments

E.S. acknowledges partial financial support from DICYT regular (042631SD_REG) and FONDEF (Grant ID25I10641). L.M.P. acknowledges partial financial support from FONDECYT (Grant ID 1240985) and Centers of Excellence with BASAL/ANID (CIA250002, CEDENNA). M.A. acknowledges financial support from the Ministry of Higher Education, Research, and Innovation (MoHERI), Sultanate of Oman, under the Block Funding Program (Agreement No. BFP/RGP/ICT/23/032). H. Vigo-Cotrina acknowledges financial support from Universidad Privada del Norte, Perú, under Project No 20241014.

Data availability statement

The data that support the findings of this study are available from the corresponding author upon reasonable request. The dataset is derived from micromagnetic simulations and requires additional post-processing for frequency-domain analysis and spatial mode visualization. Providing the data upon request allows us to offer appropriate guidance to ensure correct interpretation and reproducibility of the results.

Author contributions

Eduardo Saavedra 0000-0002-2842-2526
Conceptualization (equal), Investigation (equal), Methodology (equal), Writing – original draft (equal)

Ulises Guevara 0000-0001-7008-7357
Conceptualization (equal), Investigation (equal), Writing – original draft (equal)

Helmunt Vigo-Cotrina 0000-0003-4335-8777
Investigation (equal), Methodology (equal), Validation (equal)

Mohammed Al Bahri 0000-0001-6051-5143
Investigation (equal), Methodology (equal), Validation (equal)

Tamara González-Vega 0000-0001-8120-1231
Investigation (equal), Validation (equal)

Laura M Pérez 0000-0002-2915-309X
Funding acquisition (equal), Investigation (equal), Validation (equal)

References

[1] Goolaup S, Ramu M, Murapaka C and Lew W S 2015 *Sci. Rep.* **5** 9603
[2] Al Bahri M, Al-Kamiyani S, Al Hinaai M M and Ali N 2025 *Symmetry* **17** 1184
[3] Saavedra E, Guevara U, González-Vega T, Díaz P and Laroze D 2025 *Phys. Scr.* **100** 105953
[4] Vilsmeier F, Taniguchi T, Lindner M, Riedel C and Back C 2025 *Appl. Phys. Lett.* **127** 162405
[5] Cowburn R P and Welland M E 2000 *Science* **287** 1466–8
[6] Allwood D A, Xiong G, Faulkner C C, Atkinson D, Petit D and Cowburn R P 2005 *Science* **309** 1688–92
[7] Kläui M 2008 *J. Phys.: Condens. Matter* **20** 313001
[8] Vermeulen B B, Sorée B, Couet S, Temst K and Nguyen V D 2024 *Micromachines* **15** 696
[9] Navarro Vilca S R, Urcia Romero S R and Vigo Cotrina H E 2025 *ACS Applied Electronic Materials* **7** 3432–8
[10] Ummelen F, Swagten H and Koopmans B 2017 *Sci. Rep.* **7** 833
[11] Jeon J C, Migliorini A, Fischer L, Yoon J and Parkin S S P 2024 *ACS Nano* **18** 14507–13
[12] Bogart L K, Eastwood D S and Atkinson D 2008 *J. Appl. Phys.* **104** 33904
[13] Soledade P R, Brandõ J, Mello A and Sampaio L C 2017 *Mater. Res. Express* **4** 025034
[14] Bogart L K, Atkinson D, O'Shea K, McGrouther D and McVitie S 2009 *Phys. Rev. B* **79** 054414
[15] Gao Y *et al* 2016 *Sci. Rep.* **6** 32617
[16] Choe S B 2008 *J. Magn. Magn. Mater.* **320** 1112–4
[17] Sandweg C W, Wiese N, McGrouther D, Hermsdoerfer S J, Schultheiss H, Leven B, McVitie S, Hillebrands B and Chapman J N 2008 *J. Appl. Phys.* **103** 093906
[18] Shiu D S, Lai K F, Liu Y Y, Li Y T, Gao Z E, Kao Y M, Wu J C and Horng L 2021 *Journal of Physics Communications* **5** 075014
[19] Ho L D A, Tran M T, Cao X H, Dao V A, Ngo D T and Hoang D Q 2018 *RSC Adv.* **8** 14539–51
[20] Corona R M, Aranda A, Palma J L, Lopez C E and Escrig J 2014 *Appl. Phys. Lett.* **105** 082406
[21] Corona R, Castillo-Sepúlveda S, Altbir D and Escrig J 2021 *Curr. Appl Phys.* **21** 180–3
[22] Saavedra E, Vigo-Cotrina H, Saji C, Laroze D and Escrig J 2025 *Appl. Phys. Lett.* **127**
[23] Saavedra E, Sarria F, Mejias A, Pereira A and Escrig J 2025 *Appl. Phys. Lett.* **126** 202401
[24] Saavedra E, Terruzzi P, Palma J L and Escrig J 2025 *J. Magn. Magn. Mater.* **622** 172939
[25] Jain S, Wang C C and Adeyeye A O 2008 *Nanotechnology* **19** 085302
[26] Sun J, Jiang A Q and Sharma P 2023 *ACS Applied Electronic Materials* **5** 4692–703
[27] Foerster M, Boulle O, Esefelder S, Mattheis R and Kläui M 2016 *Domain Wall Memory Device* (Springer) 1387–441 doi:10.1007/978-94-007-6892-5_48
[28] Ho P, Tu K H, Zhang J, Sun C, Chen J, Liontos G, Ntetsikas K, Avgeropoulos A, Voyles P M and Ross C A 2016 *Nanoscale* **8** 5358–67
[29] Li J, Zhang S, Grigas C, Misra R, Bartell J, Crespi V H and Schiffer P 2012 *AIP Adv.* **2** 012136
[30] Scholl A *et al* 2000 *Science* **287** 1014–6
[31] Donnelly C and Scagnoli V 2020 *J. Phys.: Condens. Matter* **32** 213001
[32] Wartelle A *et al* 2017 *Nanotechnology* **29** 045704
[33] Vansteenkiste A, Leliaert J, Dvornik M, Helsen M, Garcia-Sanchez F and Van Waeyenberge B 2014 *AIP Adv.* **4** 107133
[34] Broens M I, Saavedra E, Bajales N, Laroze D and Escrig J 2024 *Appl. Phys. Lett.* **124** 182403

[35] Castaño F J, Ross C A, Frandsen C, Eilez A, Gil D, Smith H I, Redjdal M and Humphrey F B 2003 *Phys. Rev. B* **67** 184425
[36] Sasaki I, Nakatani R, Endo Y, Kawamura Y, Yamamoto M, Takenaga T, Aya S, Kuroiwa T, Beysen S and Kobayashi H 2006 *J. Appl. Phys.* **99** 08G303
[37] Yang S, Zhao Y, Wu K, Chu Z, Xu X, Li X, Åkerman J and Zhou Y 2023 *Nat. Commun.* **14** 3406
[38] Baker A *et al* 2017 *J. Magn. Magn. Mater.* **421** 428–39
[39] Chernyshenko D 2016 Computational methods in micromagnetics *Ph.D. thesis University of Southampton*
[40] Fullerton J, Hierro-Rodriguez A, Donnelly C, Sanz-Hernández D, Skoric L, MacLaren D A and Fernández-Pacheco A 2023 *Nanotechnology* **34** 125301
[41] Kumar D and Adeyeye A O 2017 *J. Phys. D: Appl. Phys.* **50** 343001
[42] Martinez A, Firpo F, Guevara U, Laroze D and Saavedra E 2025 *Phys. Scr.* **100** 065972
[43] Majumder S, Choudhury S, Barman S, Otani Y and Barman A 2024 *Phys. Scr.* **99** 025935
[44] Kumar Pal P and Barman A 2023 *J. Magn. Magn. Mater.* **588** 171431
[45] Jalali M, Chen Q, Tang X, Guo Q, Liang J, Zhou X, Zhang D, Huang Z and Zhai Y 2024 *Materials* **17** 2404
[46] Zhang G F, Li Z X, Wang X G, Nie Y Z and Guo G H 2015 *J. Magn. Magn. Mater.* **385** 402–6
[47] Zhang G F, Li Z X, Wang X G, Nie Y Z and Guo G H 2015 *Chin. Phys. B* **24** 097503
[48] Massouras M, Perna S, D'Aquino M, Serpico C and Kim J V 2024 *Phys. Rev. B* **110** 064435
[49] Tian C, Chaudhuri U, Singh N and Adeyeye A O 2020 *Nanotechnology* **31** 145714
[50] Saavedra E, Riveros A and Palma J L 2021 *Sci. Rep.* **11** 14230